


Competition-induced sign reversal of Casimir-Lifshitz torque: Investigation of topological nodal-line semimetals

Liang Chen ^{1,2,3,*} and Xuan Guo^{1,2}¹*School of Mathematics and Physics, North China Electric Power University, Beijing 102206, China*²*Institute of Condensed Matter Physics, North China Electric Power University, Beijing 102206, China*³*Hebei Key Laboratory of Physics and Energy Technology, North China Electric Power University, Baoding 071003, China*

(Received 9 August 2022; accepted 16 March 2023; published 27 March 2023)

The dispersion of quasiparticles in topological nodal-line semimetals is significantly different in different directions. In a certain direction, the quasiparticles behave like relativistic particles with constant velocity. In other directions, they act as two-dimensional electron gas. The competition between relativistic and non-relativistic dispersions can induce a sign reversal of Casimir-Lifshitz torque. Three different approaches can be applied to generate this sign reversal, i.e., tuning the anisotropic parameter or chemical potential in a nodal-line semimetal, and changing the distance between this material and substrate birefringence. Detailed calculations are illustrated for the system with topological nodal-line semimetal Ca_3P_2 and liquid crystal material 4-cyano-4-*n*-pentylcyclohexane-phenyl.

DOI: [10.1103/PhysRevB.107.115154](https://doi.org/10.1103/PhysRevB.107.115154)

I. INTRODUCTION

The Casimir effect [1–3] is a pure quantum phenomenon of a vacuum. This effect demonstrates that the zero-point quantum fluctuation of the electromagnetic field can result in a force between two neutral plates on the mesoscopic and nanoscopic scales. The Casimir effect plays a vital role in micro- and nanoelectromechanical systems and dominates the fabrication and performance of devices in these systems [4–8].

The Casimir-Lifshitz torque (CLT) is another related effect, which considers not only the zero-point energy fluctuation but also the angular momentum of virtual photons. The analytical description of CLT between uniaxially anisotropic half spaces was established by Barash [9,10]. In subsequent investigations, CLT for different birefringent materials has been studied [11–19]. Ingenious experiments have been proposed to measure CLT, such as utilizing the reorientation of liquid crystal nematics [15] and using an optically levitated nanorod [20]. The precision measurement in the system with liquid crystal 4-yano-4'-pentylbiphenyl (5CB) and birefringent material demonstrates the existence of CLT [21]. CLT provides an additional approach for the manipulation of Casimir physics and has substantial potential applications, such as noncontact gears [22,23], torsional Casimir actuation [24,25], Casimir rotors [26], noncontact transfer of angular momentum at nanoscale [27], etc. The sign of CLT for a fixed twisting angle may depend on the distance. Recent works give systematic investigations on the sign reversal of CLT between black phosphorus and birefringent materials [28–30]. However, it is still an open question whether there is a systematic method to find appropriate materials for the observation of CLT sign

reversal. In this paper, we study the CLT between a topological nodal-line semimetal (TNLSM) and a liquid crystal. We demonstrate that the distinct band structure and dispersion of TNLSM provide a natural mechanism for realizing the CLT sign reversal.

TNLSM [31] is a special material in which the Fermi surface is a nodal line in the three-dimensional Brillouin zone. First-principles calculations show that TNLSM can exist in various materials [32–43]. Recent experimental measurements show evidence of TNLSM in candidates PbTaSe_2 [44], ZrSiSe and ZrSiTe [45], TiB_2 [46], CaAgAs [47], SrAs_3 [48], GdSbTe [49], and Co_2MnGa [50]. Intriguing properties, such as unique Landau energy level [51], special collective modes [52], long-range Coulomb interactions [53], drumheadlike surface states [36,37], etc., make TNLSM attract great attention. Condensed matter materials provide excellent platforms for the experimental observation of novel properties of relativistic particles, e.g., Klein tunneling [54,55], Veselago lenses [56], chiral anomalies [57–59], etc. TNLSM is an even more interesting material where the bulk quasiparticles possess both the properties of relativistic and nonrelativistic particles; i.e., in some directions, the current operator is proportional to the wave vector, and in the other direction the current operator is proportional to a material-dependent *relativistic* velocity. To the best of our knowledge, physical implications which focus on these significant differences have not been reported. The sign reversal of CLT between TNLSM and birefringence is a physical consequence of this property.

II. THEORETICAL MODEL

We consider the CLT between a liquid crystal material 4-cyano-4-*n*-pentylcyclohexane-phenyl (5PCH) and a TNLSM, as shown in the upper left inset of Fig. 1. The surfaces of 5PCH and TNLSM are located at $y = 0$ and $y = a$,

*Corresponding author: slchern@ncepu.edu.cn

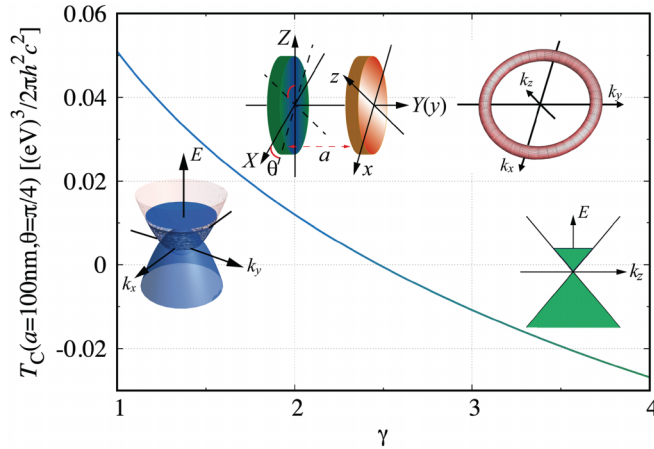


FIG. 1. Changing the anisotropic parameter γ induced sign reversal of CLT at twisting angle $\theta = \pi/4$ and fixed distance $a = 100$ nm. Other parameters for numerical calculation: $\varepsilon_0 = 0.184$ eV refers to the energy of quasiparticles on the nodal line, chemical potential $\mu = 0.5\varepsilon_0$, damping parameter $\hbar\eta = 0.05\varepsilon_0$. The top left inset shows the geometry of the Casimir interaction between 5PCH and TNLSM. The axes frames $(\hat{X}, \hat{Y}, \hat{Z})$ and $(\hat{x}, \hat{y}, \hat{z})$ are pinned to the principal directions of 5PCH (green) and TNLSM (orange), respectively. The top right inset shows the nodal line loop structure in the Brillouin zone. The lower insets show nonrelativistic (E vs k_x-k_y) and relativistic (E vs k_z) dispersions of quasiparticles. These two distinguished dispersions dominate the Casimir torque for anisotropic parameters $\gamma \ll 1$ and $\gamma \gg 1$, respectively.

respectively. The axes $(\hat{X}, \hat{Y}, \hat{Z})$ and $(\hat{x}, \hat{y}, \hat{z})$ are fixed to the principal directions of 5PCH and TNLSM, respectively. θ is the twisting angle between \hat{X} and \hat{x} . The nodal line signature of TNLSM in the wave-vector space is illustrated in the upper right inset, where the nodal line is located in the $k_z = 0$ plane.

The Casimir-Lifshitz torque per unit area is

$$T_C(a, \theta) = -\frac{\partial E_C(a, \theta)}{\partial \theta}, \quad (1)$$

where $E_C(a, \theta)$ is the corresponding Casimir energy density. At finite temperature, it takes the following form according to the Casimir-Lifshitz formula [15, 18]:

$$E_C = \frac{k_B T}{4\pi^2} \sum_{n=0}^{\infty} \int d\mathbf{p}_{\parallel} \log \det[\mathbb{I} - e^{-2\kappa a} \mathbb{R}_1 \mathbb{R}_2], \quad (2)$$

where k_B is Boltzmann's constant, T is the temperature, \mathbf{p}_{\parallel} is the electromagnetic field wave vector parallel to the interface, $\kappa = \sqrt{\mathbf{p}_{\parallel}^2 + \zeta_n^2/c^2}$, $\zeta_n = 2n\pi k_B T$ is the Matsubara frequency, c is the speed of light in the vacuum, and the prime in the summation means that the term $n = 0$ contains a prefactor $1/2$. \mathbb{I} is a 2×2 identity matrix, and $\mathbb{R}_1(\mathbf{p}_{\parallel}, i\zeta_n)$ and $\mathbb{R}_2(\mathbf{p}_{\parallel}, i\zeta_n)$ are the two Fresnel coefficient matrices on the surfaces.

To obtain a systematic investigation that accommodates the influence of the anisotropic parameter, the chemical potential, and the distance, we choose the following SU(2) spin-rotation symmetric two-orbital low energy effective model to describe the specific dispersion of quasiparticles in TNLSM

[53, 60, 61]:

$$\hat{H} = \frac{\hbar^2}{2m} (k_x^2 + k_y^2 - k_0^2) \hat{\tau}_x + \hbar v_z k_z \hat{\tau}_y, \quad (3)$$

where \hbar is the reduced Planck's constant, m is the effective mass of the quasiparticles in the xy plane, k_0 is the radius of the nodal line loop in the Brillouin zone, v_z is the Fermi velocity along the z axis, and $\hat{\tau}_x$ and $\hat{\tau}_y$ are the two Pauli matrices acting on the orbital degree of freedom. This model reveals the unique Fermi surface of TNLSM and has been used to study the influence of long-range Coulomb interaction [53], the optical properties [60], and the quantum anomalies [61] in this semimetal. In the following context, we reveal sign reversal of CLT at zero temperature. We have calculated CLT at finite temperature by considering both the thermal corrections of permittivity functions and the finite temperature distribution of virtual photons. We find that the finite-temperature corrections can be neglected here.

III. PERMITTIVITY FUNCTIONS

A systematic investigation of the optical conductivity in TNLSM was presented in Ref. [60]. From the real part of the optical conductivities, we can evaluate the imaginary part of the permittivity functions [62, 63]:

$$\text{Im}[\varepsilon_{\alpha\alpha}(\omega)] = \frac{4\pi}{\omega} \text{Re}[\sigma_{\alpha\alpha}(\omega)], \quad (4)$$

where $\alpha = x, y, z$ refer to different principal axes. Taking the Kramers-Kronig transformation,

$$\mathcal{K}[\varepsilon_{\alpha\alpha}(\omega)] = \frac{2}{\pi} \int_0^{\infty} \frac{\omega \text{Im}[\varepsilon_{\alpha\alpha}(\omega)]}{\omega^2 + \zeta^2} d\omega, \quad (5)$$

we can obtain the permittivity functions expressed in imaginary-time formalism:

$$\varepsilon_{\alpha\alpha}(i\zeta) = 1 + \mathcal{K}[\varepsilon_{\alpha\alpha}^D(\omega)] + \mathcal{K}[\varepsilon_{\alpha\alpha}^I(\omega)], \quad (6)$$

where the superscripts D and I indicate, respectively, the intraband (Drude) and interband contributions of the two-orbital model (3). For the intraband contribution, we have

$$\mathcal{K}[\varepsilon_{\alpha\alpha}^D(\omega)] = \frac{g_{\alpha\alpha}^D}{\zeta(\zeta + \eta)}, \quad (7)$$

where η is the damping parameter and $g_{\alpha\alpha}^D$ is the Drude weight. $g_{\alpha\alpha}^D$ take the following forms at zero temperature:

$$g_{xx}^D = \frac{2e^2 k_0 \mu}{\gamma \hbar^2} \left\{ 1 + \frac{1}{\pi} \left[\frac{1}{3} \tan \varphi (4 - \cos^2 \varphi) - \varphi \right] \right\}, \quad (8)$$

$$g_{yy}^D = g_{xx}^D, \quad (9)$$

$$g_{zz}^D = \frac{e^2 \gamma k_0 \mu}{\hbar^2} \left[1 + \frac{1}{\pi} \left(\frac{1}{2} \sin 2\varphi - \varphi \right) \right], \quad (10)$$

where $e^2 = 4\pi/137$ is the fine structure constant, $\gamma = 2mv_z/\hbar k_0$ describes the spatial anisotropy of the band structure, μ is the chemical potential, $\varphi = \Theta(\mu - \varepsilon_0) \cos^{-1}(\varepsilon_0/\mu)$, $\varepsilon_0 = \hbar^2 k_0^2/2m$ defines an energy scale for calculation, and $\Theta(\mu - \varepsilon_0)$ is the Heaviside step function. The interband terms take different forms from the standard Ninham-Parsegian

oscillator model [64]. Their explicit expressions are given by

$$\begin{aligned} \mathcal{K}[\varepsilon_{xx}^I(\omega)] = \mathcal{K}[\varepsilon_{yy}^I(\omega)] = & \frac{e^2 k_0}{\gamma} \frac{1}{\hbar \zeta} \left\{ \tan^{-1} \frac{\hbar \zeta}{2\mu} - \frac{1}{2} \tan^{-1} \left[\frac{\hbar \zeta}{2 \max(\mu, \varepsilon_0)} \right] + \frac{1}{\pi} \frac{\varepsilon_0}{\hbar \zeta} \log \left[1 + \left(\frac{\hbar \zeta}{2 \max(\mu, \varepsilon_0)} \right)^2 \right] - T_{\text{contour}1} \right\} \\ & - \frac{e^2 k_0}{\gamma} \frac{1}{3\pi \varepsilon_0} \left[\Theta(\mu - \varepsilon_0) \left(\log \frac{\mu + \sqrt{\mu^2 - \varepsilon_0^2}}{\varepsilon_0} + \frac{\sqrt{4\varepsilon_0^2 + \hbar^2 \zeta^2}}{2\hbar \zeta} \log \frac{\sqrt{4\varepsilon_0^2 + \hbar^2 \zeta^2}/\hbar \zeta - \sqrt{\mu^2 - \varepsilon_0^2}/\mu}{\sqrt{4\varepsilon_0^2 + \hbar^2 \zeta^2}/\hbar \zeta + \sqrt{\mu^2 - \varepsilon_0^2}/\mu} \right) - T_{\text{contour}2} \right] \\ & + \frac{e^2 k_0}{\gamma} \frac{2\varepsilon_0}{3\pi \hbar^2 \zeta^2} \left[\Theta(\mu - \varepsilon_0) \left(\frac{\sqrt{\mu^2 - \varepsilon_0^2}}{\mu} + \frac{\sqrt{4\varepsilon_0^2 + \hbar^2 \zeta^2}}{2\hbar \zeta} \log \frac{\sqrt{4\varepsilon_0^2 + \hbar^2 \zeta^2}/\hbar \zeta - \sqrt{\mu^2 - \varepsilon_0^2}/\mu}{\sqrt{4\varepsilon_0^2 + \hbar^2 \zeta^2}/\hbar \zeta + \sqrt{\mu^2 - \varepsilon_0^2}/\mu} \right) - T_{\text{contour}3} \right], \end{aligned} \quad (11)$$

$$\begin{aligned} \mathcal{K}[\varepsilon_{zz}^I(\omega)] = & \frac{e^2 \gamma k_0}{2} \frac{1}{\hbar \zeta} \left\{ \tan^{-1} \frac{\hbar \zeta}{2\mu} - \frac{1}{2} \tan^{-1} \left[\frac{\hbar \zeta}{2 \max(\mu, \varepsilon_0)} \right] + \frac{1}{\pi} \frac{\varepsilon_0}{\hbar \zeta} \log \left[1 + \left(\frac{\hbar \zeta}{2 \max(\mu, \varepsilon_0)} \right)^2 \right] - T_{\text{contour}1} \right\} \\ & - e^2 \gamma k_0 \frac{\varepsilon_0}{\pi \hbar^2 \zeta^2} \left[\Theta(\mu - \varepsilon_0) \left(\frac{\sqrt{\mu^2 - \varepsilon_0^2}}{\mu} + \frac{\sqrt{4\varepsilon_0^2 + \hbar^2 \zeta^2}}{2\hbar \zeta} \log \frac{\sqrt{4\varepsilon_0^2 + \hbar^2 \zeta^2}/\hbar \zeta - \sqrt{\mu^2 - \varepsilon_0^2}/\mu}{\sqrt{4\varepsilon_0^2 + \hbar^2 \zeta^2}/\hbar \zeta + \sqrt{\mu^2 - \varepsilon_0^2}/\mu} \right) - T_{\text{contour}3} \right], \end{aligned} \quad (12)$$

where the contour term $T_{\text{contour}1}$ takes the form of the other terms in the curly brackets with the denominators 2μ and $2 \max(\mu, \varepsilon_0)$ being replaced by the energy cutoff Λ , the contour terms $T_{\text{contour}2}$ and $T_{\text{contour}3}$ take the forms of the terms in the parentheses with μ being replaced by $\Lambda/2$. One can find that all of these contour terms are logarithmically dependent on the cutoff Λ . In the following investigation, we choose $\Lambda = 10\varepsilon_0$.

The competition between relativistic and nonrelativistic dispersions of quasiparticles can be altered by tuning the anisotropic parameter γ . For both the intraband and interband contributions, we find the following results. In one strong anisotropy limit $\gamma \rightarrow 0$, the nonrelativistic property of TNLSM dominates, both $\mathcal{K}[\varepsilon_{xx}^D(\omega)]$ and $\mathcal{K}[\varepsilon_{xx}^I(\omega)]$ tend to infinity, while $\mathcal{K}[\varepsilon_{zz}^D(\omega)]$, $\mathcal{K}[\varepsilon_{zz}^I(\omega)] \rightarrow 0$. The material tends to the ideal metallic grating limit [14,16,19], i.e., $\varepsilon_{xx} \gg \varepsilon_{zz}$. In the other strong anisotropy limit $\gamma \rightarrow \infty$, we get the opposite result, $\varepsilon_{xx} \ll \varepsilon_{zz}$. Changing the value of γ from zero to infinity behaves like a $\pi/2$ rotation of the principal axes of TNLSM. This can drive the CLT to change sign. Figure 1 shows CLT at twisting angle $\theta = \pi/4$ and distance $a = 100$ nm as a function of the anisotropic parameter γ (see the following context and the Appendix for details). We find that CLT changes sign at $\gamma \approx 2.5$ for the given parameters.

Changing the chemical potential, μ , is another appropriate approach to realize the CLT sign reversal. From Eqs. (8) and (10), we find that when $\gamma > \sqrt{2}$ and $\mu < \varepsilon_0$, $g_{xx}^D < g_{zz}^D$. In the other limit $\mu \gg \varepsilon_0$, we get asymptotic expressions:

$$g_{xx}^D = \frac{2e^2 k_0 \mu}{\gamma \hbar^2} \left[\frac{4}{3\pi} \frac{\mu}{\varepsilon_0} + \frac{1}{2} + \frac{1}{6\pi} \left(\frac{\varepsilon_0}{\mu} \right)^2 + \dots \right], \quad (13)$$

$$g_{zz}^D = \frac{e^2 \gamma k_0 \mu}{\hbar^2} \left[\frac{1}{2} + \frac{2}{\pi} \frac{\varepsilon_0}{\mu} - \frac{1}{3\pi} \left(\frac{\varepsilon_0}{\mu} \right)^2 + \dots \right], \quad (14)$$

such that $g_{zz}^D \ll g_{xx}^D$. There is a crossover from $g_{xx}^D < g_{zz}^D$ to $g_{xx}^D > g_{zz}^D$ as μ increases. Figure 2(a) shows $g_{xx}^D - g_{zz}^D$ as a function of the chemical potential. There is a transition at $\mu/\varepsilon_0 = 4.68$ for $\gamma = 2.8$. We need to emphasize that, although the Drude weights depend on k_0 , μ , ε_0 , and γ , the critical point μ/ε_0 where $g_{xx}^D(\mu/\varepsilon_0) = g_{zz}^D(\mu/\varepsilon_0)$ depends only on the anisotropic parameter γ . The interband contribution to the permittivity is more complicated. The sign of $\mathcal{K}[\varepsilon_{xx}^I(\omega)] - \mathcal{K}[\varepsilon_{zz}^I(\omega)]$ depends not only on the chemical potential but also on the imaginary frequency ζ . Figure 2(b) shows the numerical result of $\mathcal{K}[\varepsilon_{xx}^I(\omega)] - \mathcal{K}[\varepsilon_{zz}^I(\omega)]$ as a function of μ/ε_0 and $\hbar \zeta$. The dashed line refers to the boundary where $\mathcal{K}[\varepsilon_{xx}^I(\omega)] = \mathcal{K}[\varepsilon_{zz}^I(\omega)]$. Figures 2(c) and 2(d) show the competition of the total dielectric functions along different principal axes. In Fig. 2(e), we plot the dielectric functions of 5PCH and TNLSM for typical chemical potentials, $\mu = 3\varepsilon_0$ and $6\varepsilon_0$. When the chemical potential is smaller than a threshold [i.e., for $\gamma = 2.8$, $\mu = 4.78\varepsilon_0$ as shown in Fig. 2(d)], e.g., $\mu = 3\varepsilon_0$ as shown by the blue lines in Fig. 2(e), there is a reversal of the principal axes at $\hbar \zeta \approx 2$ eV, which is consistent with the boundary as shown in Fig. 2(d). The CLT should reverse at some distance $a_c \sim c/\zeta_c$ [28], where c is the speed of light in the vacuum, and ζ_c is the critical value of imaginary frequency where $\varepsilon_{xx}(i\zeta_c) - \varepsilon_{zz}(i\zeta_c) = 0$. In this case ($\mu = 3\varepsilon_0$), we expect $a_c \approx 100$ nm. When the chemical potential is greater than the threshold, e.g., $\mu = 6\varepsilon_0$ as shown by the red lines in Fig. 2(e), $\varepsilon_{xx}(i\zeta) - \varepsilon_{zz}(i\zeta)$ has a definite sign, like the conventional birefringent material [the gray lines in Fig. 2(e) for 5PCH]. The distance-dependent sign reversal of CLT disappears in this case.

IV. CASIMIR-LIFSHITZ TORQUE

On the basis of the above investigations on the permittivity functions, we study the CLT. We derive the

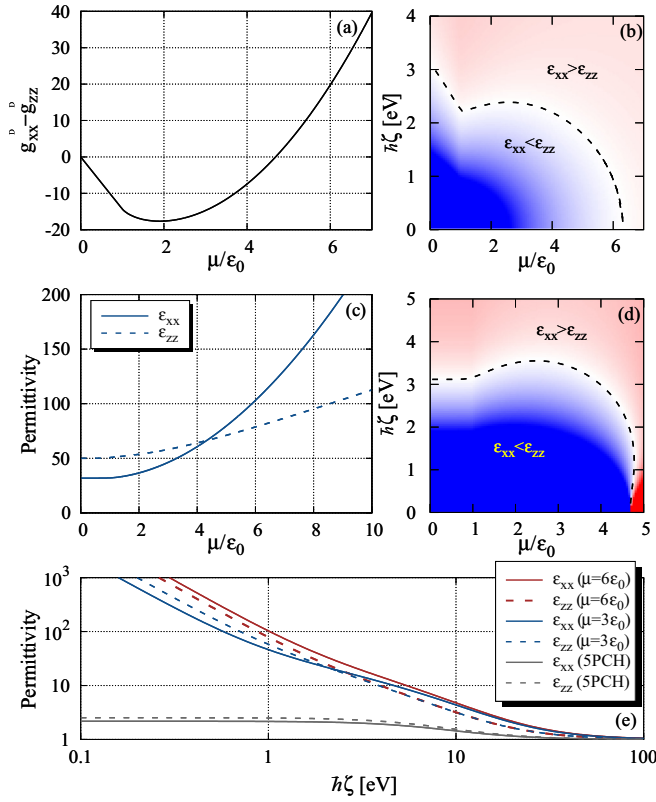


FIG. 2. Permittivity functions. (a) The difference between Drude weights, $g_{xx}^D - g_{zz}^D$, as a function of chemical potential μ . (b) $\mathcal{K}[\epsilon_{xx}^I(\omega)] - \mathcal{K}[\epsilon_{zz}^I(\omega)]$ as a function of chemical potential μ and imaginary frequency $\hbar\zeta$. (c) $\epsilon_{xx}(i\zeta)$ and $\epsilon_{zz}(i\zeta)$ given in Eq. (6) as a function of chemical potential for imaginary frequency $\hbar\zeta = 1$ eV. A cross occurs at $\mu = 4.33\epsilon_0$. (d) Contour plot of $\epsilon_{xx}(i\zeta) - \epsilon_{zz}(i\zeta)$ as a function of chemical potential and imaginary frequency. The dashed line shows the boundary where $\epsilon_{xx}(i\zeta) - \epsilon_{zz}(i\zeta) = 0$. (e) Permittivity of liquid crystal 5PCH and TNLSM ($\mu = 3\epsilon_0$ and $6\epsilon_0$, respectively) as functions of imaginary frequency. In numerical calculation, the anisotropic parameter γ has been set to be 2.8, and the energy scale ϵ_0 has been chosen to be 0.184 eV. The dielectric functions of 5PCH can be found from Refs. [65,66].

analytical expressions of the Fresnel matrices in Eq. (2) using the standard transfer matrix method [67,68]. In Cartesian coordinates,

$$\mathbf{R}_1 = (\kappa \mathbf{U}_1 - \mathbf{Q} \mathbf{V}_1)(\kappa \mathbf{U}_1 + \mathbf{Q} \mathbf{V}_1)^{-1}, \quad (15)$$

$$\mathbf{R}_2 = (\kappa \mathbf{U}_2 + \mathbf{Q} \mathbf{V}_2)(\kappa \mathbf{U}_2 - \mathbf{Q} \mathbf{V}_2)^{-1}, \quad (16)$$

where $\mathbf{Q} = \mathbf{Q}(\mathbf{p}_{\parallel}, i\zeta)$ is a 2×2 matrix that determines the propagation of the electromagnetic field in the vacuum, and \mathbf{U}_j and \mathbf{V}_j are the 2×2 submatrices of \mathbf{W}_j ($j = 1, 2$) in the following form:

$$\mathbf{W}_j = \begin{pmatrix} \mathbf{U}_j & \mathbf{U}_j \\ \mathbf{V}_j & -\mathbf{V}_j \end{pmatrix}. \quad (17)$$

The analytical expressions of \mathbf{W}_1 and \mathbf{W}_2 consist of the four eigenmodes of Maxwell's equations in 5PCH and TNLSM, respectively (see the Appendix for detailed expressions).

As shown in Fig. 2, the Drude and interband terms have significantly different contributions to the permittivity

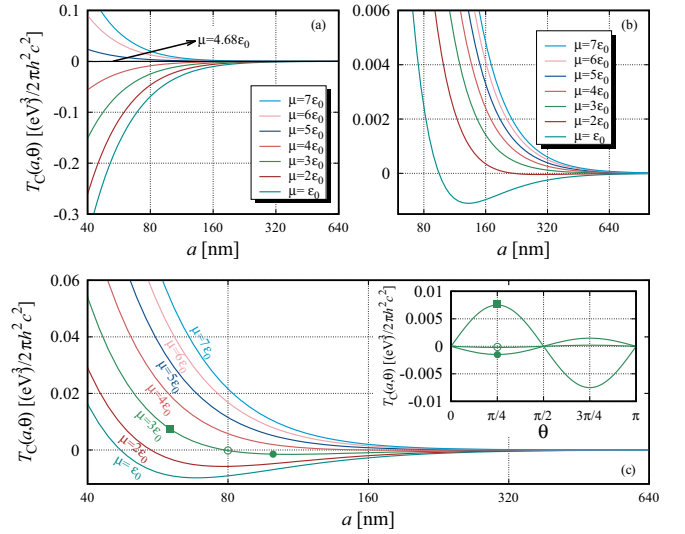


FIG. 3. Casimir-Lifshitz torque between TNLSM and 5PCH. (a) CLT as a function of distance where the permittivity functions contain only the intraband contribution. The black line shows the CLT for the isotropic situation where $g_{xx}^D(i\zeta) = g_{zz}^D(i\zeta)$. (b) CLT as a function of distance where the permittivity functions contain only the interband contribution. (c) CLT as a function of distance for different chemical potentials where the permittivity functions contain both the Drude and interband contributions. The inset shows the CLT vs twisting angle for $\mu = 3\epsilon_0$ and typical distances, $a = 60$ nm (■), 80 nm (○), and 100 nm (●).

functions. Their contributions to the CLT should be different. We consider the CLT for these terms respectively. Figures 3(a) and 3(b) show the maximal Casimir torque at $\theta = \pi/4$ as a function of distance with different chemical potentials for the Drude and interband terms, respectively. The black line for $\mu = 4.68\epsilon_0$ shows the boundary where $T_C(a, \theta)$ is exactly zero. For a lower chemical potential ($\mu < 4.68\epsilon_0$), the relativistic dispersion dominates, making the CLT negative. When $\mu > 4.68\epsilon_0$, the nonrelativistic dispersion dominates, $T_C(a, \pi/4) > 0$. The interband contributions are significantly different. In the short-distance region ($a < 80$ nm), $T_C(a, \pi/4) > 0$ for any chemical potential. This is consistent with the permittivity functions shown in Fig. 2(b), where the quadratic dispersion dominates over the linear dispersion in the large imaginary frequency region. In the large distance region, $T_C(a, \pi/4)$ is negative for chemical potential $\mu < 5\epsilon_0$. The sign of CLT reverses at some critical distance, for example, when $\mu = \epsilon_0$ the critical distance is about 85 nm. In Fig. 3(c), we plot CLT as a function of distance with both the Drude and interband contributions contained. The critical distance is 47 nm for $\mu = \epsilon_0$ and 79 nm for $\mu = 3\epsilon_0$. For fixed chemical potential $\mu = 3\epsilon_0$, the inset shows the twisting angle dependence of CLT for different distance $a = 60, 80,$ and 100 nm, respectively.

The parameters used in this paper, that is, the radius of nodal line loop k_0 , the anisotropic parameter γ , and the effective mass m , are fitted for the candidate TNLSM Ca_3P_2 [35,60]. In this paper, we consider only the low energy effective model of TNLSM, and the permittivity functions with ultraviolet (UV) optical oscillator corrections may change the

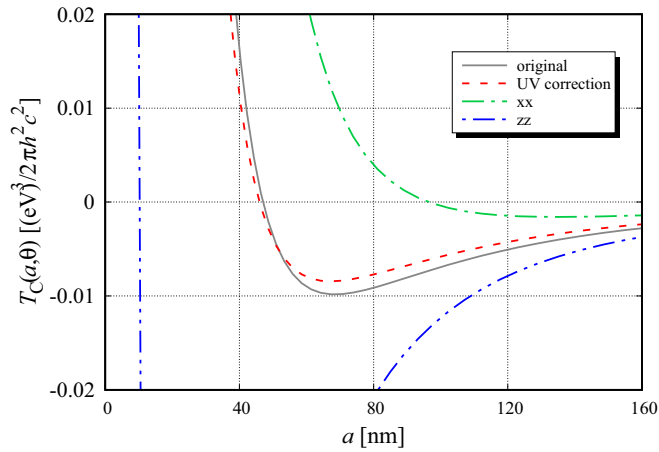


FIG. 4. UV optical oscillator corrections to the CLT. The red dashed line shows the CLT as a function of distance when the permittivity function, Eq. (4), has an additional isotropic UV optical oscillator correction, $g_{UV}/(1 + \zeta^2/\omega_{UV}^2)$, where the oscillator frequency ω_{UV} and oscillating strength g_{UV} have been set to be 3 eV and 8, respectively. For comparison, the gray (solid) line, green (dotted) line, and blue (double-dotted) line show the CLT for the following configurations: without UV optical oscillator, with UV optical oscillator for only the ϵ_{xx} component, and with UV optical oscillator for only the ϵ_{zz} component. $\mu = \epsilon_0$ in TNLSM is set in calculation.

Casimir interaction in the short-distance region. Numerical evaluation of CLT by considering the UV optical oscillator shows that the competition-induced sign reversal is valid in a wide parameter regime. In Fig. 4, we calculate CLT by considering UV optical oscillators for three different cases, i.e., both the in-plane and out-of-plane components have corrections (the red dash line), only the in-plane component has correction (the green dotted dash line), and only the out-of-plane component has correction (the blue double-dotted dash line). We find that the sign reversal appears at about 50, 90, and 10 nm for these cases, respectively. Furthermore, the critical distances in the interval 45–80 nm (shown in Fig. 3) can be further

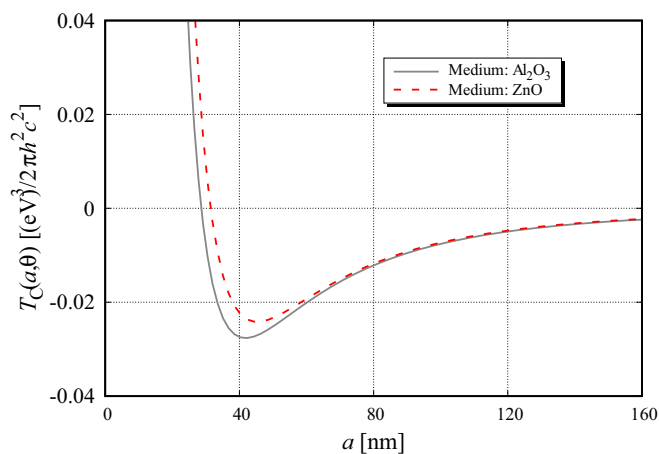


FIG. 5. CLT as a function of separation distance between 5PCH and TNLSM with intervening homogeneous layers. $\mu = \epsilon_0$ in TNLSM is set in calculation. Dielectric functions of Al_2O_3 and ZnO can be found from Ref. [69].

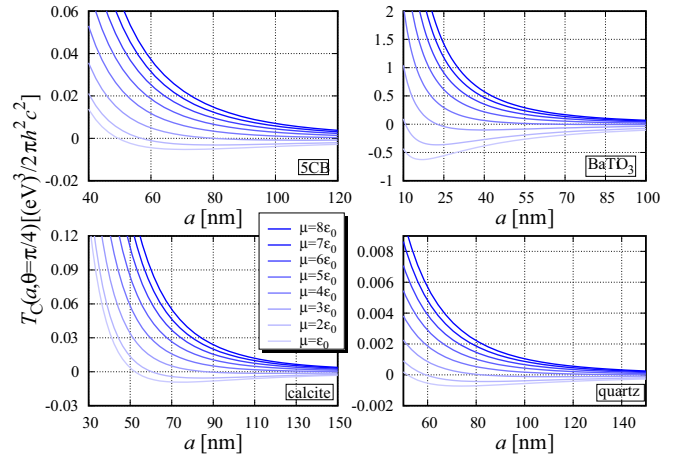


FIG. 6. 5PCH being replaced by other birefringent materials. CLT between TNLSM and other birefringent materials as a function of distance for different chemical potentials in TNLSM. The optical data of these materials, i.e., 5CB, BaTiO_3 , calcite, and quartz, can be found from Refs. [65,66,69].

reduced by intervening homogeneous dielectrics between the slabs [17,30]. Figure 5 shows CLT at $\theta = \pi/4$ as a function of distance for $\mu = \epsilon_0$ with Al_2O_3 and ZnO inserted in between 5PCH and TNLSM. The sign reversal appears at 28 and 31 nm for Al_2O_3 and ZnO intervened respectively.

The sign reversal of CLT is induced by the unique dispersion of TNLSM. The liquid crystal 5PCH can be replaced by other birefringent materials. We calculate the CLT between TNLSM and other birefringent materials, i.e., liquid crystal 5CB, inorganic materials BaTiO_3 , calcite, and quartz (see Fig. 6 for details). We find that changing the anisotropic parameter, chemical potential, and distance can reproduce the sign reversal of CLT. However, the critical point where sign reversal occurs does depend on the particular choice of the other birefringent materials in front of TNLSM.

V. CONCLUSION

In summary, we study the CLT between TNLSM and conventional birefringent materials. The distinct band structure and dispersion of TNLSM provide a precise mechanism for the sign reversal of CLT, i.e., the relative strengths of polarizabilities along different principal axes can be changed by the competition of relativistic and nonrelativistic properties of quasiparticles in TNLSM. Experimentally, this sign reversal can be manifested by changing the anisotropic parameter, the chemical potential, and the distance between TNLSM and birefringent material. Quantitative calculations show that, in the system consisting of TNLSM Ca_3P_2 and liquid crystal 5PCH, the sign reversal of CLT appears at a separation distance which is very close to the experimental accessible regime.

ACKNOWLEDGMENTS

The authors are grateful for financial support from the National Natural Science Foundation of China (Grant No. 12174101) and the Fundamental Research Funds for the Central Universities (Grant No. 2022MS051).

APPENDIX: EIGENMODES OF MAXWELL'S EQUATIONS

The analytical expression of \mathbb{Q} given in Eqs. (15) and (16) is

$$\mathbb{Q}(\mathbf{p}_{\parallel}, i\zeta) = \begin{pmatrix} -\frac{cp_x p_z}{\zeta} & \frac{\zeta}{c} + \frac{cp_z^2}{\zeta} \\ -\frac{\zeta}{c} - \frac{cp_x^2}{\zeta} & \frac{cp_x p_z}{\zeta} \end{pmatrix}. \quad (\text{A1})$$

The analytical expressions of \mathbb{U}_j and \mathbb{V}_j given in Eqs. (15) and (16) are

$$\mathbb{U}_j(\mathbf{p}_{\parallel}, i\zeta) = \begin{pmatrix} \sin \theta_j & c^2 p_z (p_x \sin \theta_j - p_z \cos \theta_j) - \zeta^2 \varepsilon_{xx}^{(j)}(i\zeta) \cos \theta_j \\ \cos \theta_j & c^2 p_x (p_x \sin \theta_j - p_z \cos \theta_j) + \zeta^2 \varepsilon_{xx}^{(j)}(i\zeta) \cos \theta_j \end{pmatrix}, \quad (\text{A2})$$

$$\mathbb{V}_j(\mathbf{p}_{\parallel}, i\zeta) = \mathbb{Q}_j \mathbb{U}_j \Lambda_j^{-1}, \quad (\text{A3})$$

where $j = 1, 2$ refer to 5PCH and TNLSM, respectively, $\varepsilon_{xx}^{(j)}(i\zeta)$ are the corresponding permittivity functions, Λ_j consists of the eigenvalues of Maxwell's equations,

$$\Lambda_j(\mathbf{p}_{\parallel}, i\zeta) = \text{diag} \left(\sqrt{\frac{\zeta^2 \varepsilon_{xx}^{(j)}(i\zeta)}{c^2} + p_x^2 + p_z^2}, \sqrt{\frac{\zeta^2 \varepsilon_{zz}^{(j)}(i\zeta)}{c^2} + (p_x \cos \theta_j + p_z \sin \theta_j)^2 + (p_x \sin \theta_j - p_z \cos \theta_j)^2 \frac{\varepsilon_{zz}^{(j)}(i\zeta)}{\varepsilon_{xx}^{(j)}(i\zeta)}} \right), \quad (\text{A4})$$

and \mathbb{Q}_j takes a similar form as Eq. (A1):

$$\mathbb{Q}_j(\mathbf{p}_{\parallel}, i\zeta) = \begin{pmatrix} -\frac{cp_x p_z}{\zeta} + \frac{\zeta}{c} [\varepsilon_{xx}^{(j)} - \varepsilon_{zz}^{(j)}] \sin \theta_j \cos \theta_j & \frac{cp_z^2}{\zeta} + \frac{\zeta}{c} [\varepsilon_{xx}^{(j)} \cos^2 \theta_j + \varepsilon_{zz}^{(j)} \sin^2 \theta_j] \\ -\frac{cp_x^2}{\zeta} - \frac{\zeta}{c} [\varepsilon_{xx}^{(j)} \sin^2 \theta_j + \varepsilon_{zz}^{(j)} \cos^2 \theta_j] & \frac{cp_x p_z}{\zeta} - \frac{\zeta}{c} [\varepsilon_{xx}^{(j)} - \varepsilon_{zz}^{(j)}] \sin \theta_j \cos \theta_j \end{pmatrix}. \quad (\text{A5})$$

-
- [1] P. W. Milonni, *The Quantum Vacuum: An Introduction to Quantum Electrodynamics* (Academic, New York, 1994).
- [2] M. Bordag, G. L. Klimchitskaya, U. Mohideen, and V. M. Mostepanenko, *Advances in the Casimir Effect* (Oxford University, New York, 2009).
- [3] G. L. Klimchitskaya, U. Mohideen, and V. M. Mostepanenko, The Casimir force between real materials: Experiment and theory, *Rev. Mod. Phys.* **81**, 1827 (2009).
- [4] H. B. Chan, V. A. Aksyuk, R. N. Kleiman, D. J. Bishop, and F. Capasso, Quantum mechanical actuation of microelectromechanical systems by the Casimir force, *Science* **291**, 1941 (2001).
- [5] H. B. Chan, V. A. Aksyuk, R. N. Kleiman, D. J. Bishop, and F. Capasso, Nonlinear Micromechanical Casimir Oscillator, *Phys. Rev. Lett.* **87**, 211801 (2001).
- [6] E. Buks and M. L. Roukes, Stiction, adhesion energy, and the Casimir effect in micromechanical systems, *Phys. Rev. B* **63**, 033402 (2001).
- [7] E. Buks and M. L. Roukes, Metastability and the Casimir effect in micromechanical systems, *Europhys. Lett.* **54**, 220 (2001).
- [8] J. Javor, Z. Yao, M. Imboden, D. K. Campbell, and D. J. Bishop, Analysis of a Casimir-driven parametric amplifier with resilience to Casimir pull-in for MEMS single-point magnetic gradiometry, *Microsyst. Nanoeng.* **7**, 73 (2021).
- [9] Y. S. Barash, Van der Waals interaction between anisotropic bodies, *Radiophys. Quantum Electron.* **16**, 945 (1973).
- [10] Y. S. Barash, Moment of van der Waals forces between anisotropic bodies, *Radiophys. Quantum Electron.* **21**, 1138 (1978).
- [11] S. J. van Enk, Casimir torque between dielectrics, *Phys. Rev. A* **52**, 2569 (1995).
- [12] J. N. Munday, D. Iannuzzi, Y. Barash, and F. Capasso, Torque on birefringent plates induced by quantum fluctuations, *Phys. Rev. A* **71**, 042102 (2005).
- [13] C.-G. Shao, A.-H. Tong, and J. Luo, Casimir torque between two birefringent plates, *Phys. Rev. A* **72**, 022102 (2005).
- [14] T. A. Morgado, S. I. Maslovski, and M. G. Silveirinha, Ultrahigh Casimir interaction torque in nanowire systems, *Opt. Express* **21**, 14943 (2013).
- [15] D. A. T. Somers and J. N. Munday, Rotation of a liquid crystal by the Casimir torque, *Phys. Rev. A* **91**, 032520 (2015).
- [16] R. Gu erout, C. Genet, A. Lambrecht, and S. Reynaud, Casimir torque between nanostructured plates, *Europhys. Lett.* **111**, 44001 (2015).
- [17] D. A. T. Somers and J. N. Munday, Casimir-Lifshitz Torque Enhancement by Retardation and Intervening Dielectrics, *Phys. Rev. Lett.* **119**, 183001 (2017).
- [18] D. A. T. Somers and J. N. Munday, Conditions for repulsive Casimir forces between identical birefringent materials, *Phys. Rev. A* **95**, 022509 (2017).
- [19] M. Antezza, H. B. Chan, B. Guizal, V. N. Marachevsky, R. Messina, and M. Wang, Giant Casimir Torque between Rotated Gratings and the $\theta = 0$ Anomaly, *Phys. Rev. Lett.* **124**, 013903 (2020).
- [20] Z. Xu and T. Li, Detecting Casimir torque with an optically levitated nanorod, *Phys. Rev. A* **96**, 033843 (2017).
- [21] D. A. T. Somers, J. L. Garrett, K. J. Palm, and J. N. Munday, Measurement of the Casimir torque, *Nature (London)* **564**, 386 (2018).
- [22] I. Cavero-Pel  ez, K. A. Milton, P. Parashar, and K. V. Shajesh, Noncontact gears. II. Casimir torque between concentric corrugated cylinders for the scalar case, *Phys. Rev. D* **78**, 065019 (2008).

- [23] A. Ashourvan, M. F. Miri, and R. Golestanian, Noncontact Rack and Pinion Powered by the Lateral Casimir Force, *Phys. Rev. Lett.* **98**, 140801 (2007).
- [24] F. Tajik, M. Sedighi, and G. Palasantzas, Sensitivity on materials optical properties of single beam torsional Casimir actuation, *J. Appl. Phys.* **121**, 174302 (2017).
- [25] F. Tajik, M. Sedighi, A. A. Masoudi, H. Waalkens, and G. Palasantzas, Dependence of chaotic behavior on optical properties and electrostatic effects in double-beam torsional Casimir actuation, *Phys. Rev. E* **98**, 022210 (2018).
- [26] J. C. Martinez, X. Chen, and M. B. A. Jalil, Casimir effect and graphene: Tunability, scalability, Casimir rotor, *AIP Adv.* **8**, 015330 (2018).
- [27] S. Sanders, W. J. M. Kort-Kamp, D. A. R. Dalvit, and A. Manjavacas, Nanoscale transfer of angular momentum mediated by the Casimir torque, *Commun. Phys.* **2**, 71 (2019).
- [28] P. Thiyam, P. Parashar, K. V. Shajesh, O. I. Malyi, M. Boström, K. A. Milton, I. Brevik, and C. Persson, Distance-Dependent Sign Reversal in the Casimir-Lifshitz Torque, *Phys. Rev. Lett.* **120**, 131601 (2018).
- [29] P. Thiyam, P. Parashar, K. V. Shajesh, O. I. Malyi, M. Boström, K. A. Milton, I. Brevik, J. Forsman, and C. Persson, Effect of excess charge carriers and fluid medium on the magnitude and sign of the Casimir-Lifshitz torque, *Phys. Rev. B* **100**, 205403 (2019).
- [30] P. Thiyam, Sign reversal of Casimir-Lifshitz torque with separation distance: A theoretical guide to experimentation, *Phys. Rev. B* **105**, 165413 (2022).
- [31] A. A. Burkov, M. D. Hook, and L. Balents, Topological nodal semimetals, *Phys. Rev. B* **84**, 235126 (2011).
- [32] J.-M. Carter, V. V. Shankar, M. A. Zeb, and H.-Y. Kee, Semimetal and topological insulator in perovskite iridates, *Phys. Rev. B* **85**, 115105 (2012).
- [33] H. Weng, Y. Liang, Q. Xu, R. Yu, Z. Fang, X. Dai, and Y. Kawazoe, Topological node-line semimetal in three-dimensional graphene networks, *Phys. Rev. B* **92**, 045108 (2015).
- [34] L. S. Xie, L. M. Schoop, E. M. Seibel, Q. D. Gibson, W. Xie, and R. J. Cava, A new form of Ca_3P_2 with a ring of Dirac nodes, *APL Mater.* **3**, 083602 (2015).
- [35] Y.-H. Chan, C.-K. Chiu, M. Y. Chou, and A. P. Schnyder, Ca_3P_2 and other topological semimetals with line nodes and drumhead surface states, *Phys. Rev. B* **93**, 205132 (2016).
- [36] R. Yu, H. Weng, Z. Fang, X. Dai, and X. Hu, Topological Node-Line Semimetal and Dirac Semimetal State in Antiperovskite Cu_3PdN , *Phys. Rev. Lett.* **115**, 036807 (2015).
- [37] Y. Kim, B. J. Wieder, C. L. Kane, and A. M. Rappe, Dirac Line Nodes in Inversion-Symmetric Crystals, *Phys. Rev. Lett.* **115**, 036806 (2015).
- [38] R. Li, H. Ma, X. Cheng, S. Wang, D. Li, Z. Zhang, Y. Li, and X.-Q. Chen, Dirac Node Lines in Pure Alkali Earth Metals, *Phys. Rev. Lett.* **117**, 096401 (2016).
- [39] J.-T. Wang, H. Weng, S. Nie, Z. Fang, Y. Kawazoe, and C. Chen, Body-Centered Orthorhombic C_{16} : A Novel Topological Node-Line Semimetal, *Phys. Rev. Lett.* **116**, 195501 (2016).
- [40] A. Yamakage, Y. Yamakawa, Y. Tanaka, and Y. Okamoto, Line-node Dirac semimetal and topological insulating phase in noncentrosymmetric pnictides CaAgX ($X = \text{P}, \text{As}$), *J. Phys. Soc. Jpn.* **85**, 013708 (2016).
- [41] Y. Du, F. Tang, D. Wang, L. Sheng, E.-j. Kan, C.-G. Duan, S. Y. Savrasov, and X. Wan, CaTe : A new topological node-line and Dirac semimetal, *npj Quantum Mater.* **2**, 3 (2017).
- [42] Q. Xu, R. Yu, Z. Fang, X. Dai, and H. Weng, Topological nodal line semimetals in the CaP_3 family of materials, *Phys. Rev. B* **95**, 045136 (2017).
- [43] S. Nie, H. Weng, and F. B. Prinz, Topological nodal-line semimetals in ferromagnetic rare-earth-metal monohalides, *Phys. Rev. B* **99**, 035125 (2019).
- [44] G. Bian, T.-R. Chang, R. Sankar, S.-Y. Xu, H. Zheng, T. Neupert, C.-K. Chiu, S.-M. Huang, G. Chang, I. Belopolski, D. S. Sanchez, M. Neupane, N. Alidoust, C. Liu, B. Wang, C.-C. Lee, H.-T. Jeng, C. Zhang, Z. Yuan, S. Jia, *et al.*, Topological nodal-line fermions in spin-orbit metal PbTaSe_2 , *Nat. Commun.* **7**, 10556 (2016).
- [45] J. Hu, Z. Tang, J. Liu, X. Liu, Y. Zhu, D. Graf, K. Myhro, S. Tran, C. N. Lau, J. Wei, and Z. Mao, Evidence of Topological Nodal-Line Fermions in ZrSiSe and ZrSiTe , *Phys. Rev. Lett.* **117**, 016602 (2016).
- [46] Z. Liu, R. Lou, P. Guo, Q. Wang, S. Sun, C. Li, S. Thirupathiah, A. Fedorov, D. Shen, K. Liu, H. Lei, and S. Wang, Experimental Observation of Dirac Nodal Links in Centrosymmetric Semimetal TiB_2 , *Phys. Rev. X* **8**, 031044 (2018).
- [47] D. Takane, K. Nakayama, S. Souma, T. Wada, Y. Okamoto, K. Takenaka, Y. Yamakawa, A. Yamakage, T. Mitsuhashi, K. Horiba, H. Kumigashira, T. Takahashi, and T. Sato, Observation of Dirac-like energy band and ring-torus Fermi surface associated with the nodal line in topological insulator CaAgAs , *npj Quantum Mater.* **3**, 1 (2018).
- [48] S. Li, Z. Guo, D. Fu, X.-C. Pan, J. Wang, K. Ran, S. Bao, Z. Ma, Z. Cai, R. Wang, R. Yu, J. Sun, F. Song, and J. Wen, Evidence for a Dirac nodal-line semimetal in SrAs_3 , *Sci. Bull.* **63**, 535 (2018).
- [49] M. M. Hosen, G. Dhakal, K. Dimitri, P. Maldonado, A. Aperis, F. Kabir, C. Sims, P. Riseborough, P. M. Oppeneer, D. Kaczorowski, T. Durakiewicz, and M. Neupane, Discovery of topological nodal-line fermionic phase in a magnetic material GdSbTe , *Sci. Rep.* **8**, 13283 (2018).
- [50] I. Belopolski, K. Manna, D. S. Sanchez, G. Chang, B. Ernst, J. Yin, S. S. Zhang, T. Cochran, N. Shumiya, H. Zheng, B. Singh, G. Bian, D. Multer, M. Litskevich, X. Zhou, S.-M. Huang, B. Wang, T.-R. Chang, S.-Y. Xu, A. Bansil *et al.*, Discovery of topological Weyl fermion lines and drumhead surface states in a room temperature magnet, *Science* **365**, 1278 (2019).
- [51] J.-W. Rhim and Y. B. Kim, Landau level quantization and almost flat modes in three-dimensional semimetals with nodal ring spectra, *Phys. Rev. B* **92**, 045126 (2015).
- [52] Z. Yan, P.-W. Huang, and Z. Wang, Collective modes in nodal line semimetals, *Phys. Rev. B* **93**, 085138 (2016).
- [53] Y. Huh, E.-G. Moon, and Y. B. Kim, Long-range Coulomb interaction in nodal-ring semimetals, *Phys. Rev. B* **93**, 035138 (2016).
- [54] A. F. Young and P. Kim, Quantum interference and Klein tunnelling in graphene heterojunctions, *Nat. Phys.* **5**, 222 (2009).
- [55] N. Stander, B. Huard, and D. Goldhaber-Gordon, Evidence for Klein Tunneling in Graphene p - n Junctions, *Phys. Rev. Lett.* **102**, 026807 (2009).
- [56] V. V. Cheianov, V. Fal'ko, and B. L. Altshuler, The Focusing of electron flow and a Veselago lens in graphene p - n junctions, *Science* **315**, 1252 (2007).

- [57] A. A. Zyuzin and A. A. Burkov, Topological response in Weyl semimetals and the chiral anomaly, *Phys. Rev. B* **86**, 115133 (2012).
- [58] X. Huang, L. Zhao, Y. Long, P. Wang, D. Chen, Z. Yang, H. Liang, M. Xue, H. Weng, Z. Fang, X. Dai, and G. Chen, Observation of the Chiral-Anomaly-Induced Negative Magnetoresistance in 3D Weyl Semimetal TaAs, *Phys. Rev. X* **5**, 031023 (2015).
- [59] C.-L. Zhang, S.-Y. Xu, I. Belopolski, Z. Yuan, Z. Lin, B. Tong, G. Bian, N. Alidoust, C.-C. Lee, S.-M. Huang, T.-R. Chang, G. Chang, C.-H. Hsu, H.-T. Jeng, M. Neupane, D. S. Sanchez, H. Zheng, J. Wang, H. Lin, C. Zhang *et al.*, Signatures of the Adler-Bell-Jackiw chiral anomaly in a Weyl fermion semimetal, *Nat. Commun.* **7**, 10735 (2016).
- [60] S. Barati and S. H. Abedinpour, Optical conductivity of three and two dimensional topological nodal-line semimetals, *Phys. Rev. B* **96**, 155150 (2017).
- [61] A. A. Burkov, Quantum anomalies in nodal line semimetals, *Phys. Rev. B* **97**, 165104 (2018).
- [62] K. L. Kliewer and R. Fuchs, Lindhard dielectric functions with a finite electron lifetime, *Phys. Rev.* **181**, 552 (1969).
- [63] H. U. Yang, J. D'Archangel, M. L. Sundheimer, E. Tucker, G. D. Boreman, and M. B. Raschke, Optical dielectric function of silver, *Phys. Rev. B* **91**, 235137 (2015).
- [64] V. A. Parsegian, *Van der Waals Forces: A Handbook for Biologists, Chemists, Engineers, and Physicists* (Cambridge University, New York, 2005).
- [65] S.-T. Wu, C.-S. Wu, M. Warengem, and M. Ismaili, Refractive index dispersions of liquid crystals, *Opt. Eng.* **32**, 1775 (1993).
- [66] P. E. Kornilovitch, Van der Waals interaction in uniaxial anisotropic media, *J. Phys.: Condens. Matter* **25**, 035102 (2013).
- [67] D. W. Berreman, Optics in stratified and anisotropic media: 4×4 -matrix formulation, *J. Opt. Soc. Am.* **62**, 502 (1972).
- [68] A. Gerrard and J. M. Burch, *Introduction to Matrix Methods in Optics* (Dover, New York, 1994).
- [69] L. Bergström, Hamaker constants of inorganic materials, *Adv. Colloid Interface Sci.* **70**, 125 (1997).